POLITECNICO DI TORINO
Repository ISTITUZIONALE

Tin-Modified MXene Composite Electrodes as Lithiophilic Hosts for Stable Lithium Metal Anodes

Original
Tin-Modified MXene Composite Electrodes as Lithiophilic Hosts for Stable Lithium Metal Anodes / Vallana, N., Gentile, A., Marchionna, S., Stievano, L., Ruffo, R.. - In: BATTERIES & SUPERCAPS. - ISSN 2566-6223. - 9:9(2026). [10.1002/batt.70466]

Availability:
This version is available at: 11583/3017154 since: 2026-10-28T14:12:07Z

Publisher:
Wiley

Published
DOI:10.1002/batt.70466

Terms of use:

This article is made available under terms and conditions as specified in the corresponding bibliographic description in the repository

Publisher copyright

(Article begins on next page)

26 November 2026

Check for updates

Batteries & Supercaps

Chemistry Europe
European Chemical Societies Publishing

Batteries & Supercaps

RESEARCH ARTICLE OPEN ACCESS

Tin-Modified MXene Composite Electrodes as Lithiophilic Hosts for Stable Lithium Metal Anodes

Nicholas Vallana[1] | Antonio Gentile[2] | Stefano Marchionna[2] | Lorenzo Stievano[3,4,5,6] | Riccardo Ruffo[1,7,8]

[1]Department of Materials Science, Università degli Studi di Milano Bicocca, Milano, Italy | [2]Ricerca sul Sistema Energetico - RSE S.p.A., Milano, Italy | [3]ICGM, Univ. Montpellier, ENSCM, CNRS, Montpellier, France | [4]Réseau sur le Stockage Electrochimique de l'Energie (RS2E), CNRS, Amiens, France | [5]ALISTORE-ERI, CNRS, Amiens, France | [6]GAME Lab, Department of Applied Science and Technology (DISAT), Politecnico di Torino, Torino, Italy | [7]National Reference Center for Electrochemical Energy Storage (GISEL), Firenze, Italy | [8]INSTM, Consorzio Interuniversitario per la Scienza e Tecnologia dei Materiali, Firenze, Italy

Correspondence: Lorenzo Stievano (lorenzo.stievano@umontpellier.fr) | Riccardo Ruffo (riccardo.ruffo@unimib.it)

Received: 5 May 2026 | **Revised:** 29 July 2026 | **Accepted:** 11 August 2026

Keywords: lithium deposition | lithium metal batteries | lamellar structures | MXene | Sn

ABSTRACT

Lithium metal anodes provide a tenfold higher theoretical capacity than graphite but face issues such as dendritic growth, unstable solid–electrolyte interphases (SEIs), large volume changes, and "dead" lithium formation, which limit their practical application. In this work, a Sn-modified $Ti_3C_2T_x$ MXene host (Sn@MX) is introduced to combine the lamellar architecture of MXene with Sn-derived lithiophilic sites, enabling controlled lithium deposition. The Sn@MX material was prepared through precursor-assisted expansion of MXene lamellae followed by incorporation of Sn-containing species. Electrochemical testing using the reservoir method shows that Sn@MX maintains stable plating and stripping for over 120 cycles at 1 mA cm^{-2}, unlike copper and untreated MXene electrodes, which fail rapidly. Ex situ and *operando* optical microscopy indicate that lithium preferentially deposits within the Sn@MX electrode structure, resulting in more uniform deposition and reduced dendritic growth. These results emphasize the importance of combining porous lamellar architectures with lithiophilic sites to develop stable lithium metal anodes for advanced batteries.

1 | Introduction

Among the various energy storage technologies, rechargeable batteries represent a key solution because of their ability to store and deliver energy on demand with high efficiency. At present, lithium-ion batteries (LIBs) dominate the rechargeable battery market [1] thanks to their high energy density, long cycle life, and well-established manufacturing infrastructure, which makes them essential for portable electronics, electric vehicles, and grid-scale energy storage systems [2]. However, LIBs are approaching their theoretical energy density limit, which is constrained by the specific capacity of graphite anodes (372 mAh g^{-1}) [3, 4]. In addition to this limitation, one of the most pressing concerns is safety: under fast-charging conditions or prolonged cycling, Li plating may occur on the graphite anode, leading to the formation of dendritic Li [5]. This intrinsic drawback poses challenges for the development of next-generation, high-energy lithium batteries. A promising alternative to meet this demand is represented by lithium metal batteries (LMBs) using metallic Li as the anode, which offers a much higher theoretical capacity (3860 mAh g^{-1}) compared to graphite [6–8], as well as the lowest electrochemical potential among all metal anodes (−3.04 V vs. SHE) [9]. By replacing graphite with Li metal, batteries can potentially achieve substantially higher energy densities, making them attractive for a broad range of applications, such as long-range electric vehicles, aerospace technologies, and grid-scale storage [10]. However, realizing the full potential of LMBs requires overcoming critical challenges such as dendrite growth, volume expansion, and interfacial instability, which severely compromise cycle life and safety [11].

This is an open access article under the terms of the Creative Commons Attribution-NonCommercial License, which permits use, distribution and reproduction in any medium, provided the original work is properly cited and is not used for commercial purposes.

© 2026 The Author(s). *Batteries & Supercaps* published by Wiley-VCH GmbH.

A major issue is, indeed, the formation of Li dendrites during repeated plating and stripping cycles. These dendrites can penetrate the separator, causing internal short circuits that may trigger thermal runaway and even battery fires [12]. In addition, dendritic growth consumes active Li, thereby accelerating performance degradation. Another challenge lies in the significant volume changes associated with Li deposition and dissolution [13]. Unlike intercalation-based anodes, Li metal undergoes virtually unlimited expansion and contraction, leading to mechanical instability at the electrode–electrolyte interface [14]. This instability disrupts the solid–electrolyte interphase (SEI), resulting in increased side reactions and electrolyte consumption. Problems such as dendrite growth, "dead" Li formation, unstable SEI layers, and parasitic reactions are highly interconnected [15, 16]. For instance, dendrite growth can break the SEI, further amplifying electrolyte decomposition and active-Li consumption. Accordingly, recent studies on metal-anode systems have emphasized that controlling interfacial chemistry, ion solvation, and the electrical double layer is crucial for regulating metal nucleation and suppressing unstable growth [17]. To address these issues, intensive research has focused on materials and structural strategies [18, 19] including artificial SEI design [20–22], anode structural engineering [23–25], electrolyte optimization (including electrolyte additives, quasi-solid-state and solid-state electrolytes) [26–32], and separator modification [33]. Collectively, these approaches aim to produce safer and longer-lasting LMBs, facilitating their transition from laboratory studies to real-world applications in high-energy storage systems.

Conventional copper (Cu) foils, employed as current collectors (CCs) in LMBs, face intrinsic limitations arising from their planar geometry [34]. Their flat surface promotes heterogeneous Li-ion flux during plating, resulting in localized hotspots and accelerated dendrite formation under high current densities [35]. This uneven ion distribution fosters dendritic Li growth and the accumulation of electrochemically inactive "dead" Li, reducing Coulombic efficiency and increasing safety risks. Furthermore, the limited surface area of 2D Cu CCs cannot effectively buffer the volume changes that occur during cycling, leading to stress accumulation, electrode pulverization, and capacity fading [36]. A promising strategy to address these shortcomings is the use of three-dimensional (3D) host structures to accommodate Li metal anodes. The high surface area of 3D scaffolds reduces local current density, delays dendrite formation, and mitigates volume fluctuations [37]. To date, various types of 3D scaffolds have been investigated as host structures for Li metal anodes [38–42], effectively reducing current density, confining Li within pores, and suppressing dendritic growth. In contrast to porous matrices that primarily mitigate volume expansion at the microscale, lamellar host materials offer tunable interlamellar spaces. This enables accommodation of Li metal within the lamellar morphology, while controlling nucleation and growth at the nanoscale [43]. In addition to the overall host geometry, recent studies have also shown that lithiophilic alloy interfaces and local curvature effects in 3D current collectors can regulate the electric field and Li-ion flux, guiding selective Li nucleation and growth [42, 44].

Among these, MXenes, a family of 2D transition metal carbides and nitrides, have attracted significant attention due to their remarkable physical and chemical properties [45]. They are typically synthesized by etching the A-group element from MAX phases (where M is an early transition metal, A is a group 13 or 14 element, and X is C or N) using hydrofluoric acid or other etchant conditions [46]. Since their discovery, MXenes have been investigated for a wide range of applications, including energy storage [47–50], electrocatalysis, photocatalysis [51–53], hydrogen storage and production [54, 55], biosensing [56, 57], and water purification [58, 59]. Recent work has further highlighted the importance of controlling interfacial chemistry, ion solvation, the electrical double layer, and SEI stability to regulate metal nucleation and suppress unstable growth, while also showing that the rich and tunable surface chemistry of MXenes can be exploited to regulate ion storage and interfacial processes in emerging battery chemistries [60, 61].

As Li tends to deposit directly on the MXene surface rather than within the interlamellar spaces, uncontrolled surface growth and dendrite formation may be favored. Recent studies on MXene-based hosts, however, have shown that interfacial MXene engineering can guide lamellar Li nucleation and suppress dendritic growth, highlighting the relevance of MXene surface chemistry and layered architectures for Li metal anodes [62]. Moreover, to promote Li nucleation and deposition within the lamellar architecture, lithiophilic species such as tin (Sn) [63, 64] can also be introduced [65]. Sn-based species are widely regarded as lithiophilic sites because they interact favorably with lithium and, upon electrochemical activation, form Li-Sn alloys [66]. These features effectively lower the lithium nucleation barrier and promote a more homogeneous lithium deposition within the host structure.

This work reports a Sn-modified $Ti_3C_2T_x$ MXene composite electrode (Sn@MX) as a promising host for Li metal anodes (Figure 1). The combination of the lamellar MXene architecture with the Sn-derived lithiophilic sites promotes homogeneous and spatially confined Li plating during cycling, effectively mitigating dendritic growth. The composite material was synthesized by reacting MXene with $SnCl_4$ in an aqueous solution, using a pillarizing/expanding agent to facilitate the incorporation of Sn-containing species within the lamellar structure. X-ray diffraction (XRD) confirmed the expansion of the MXene interlayer

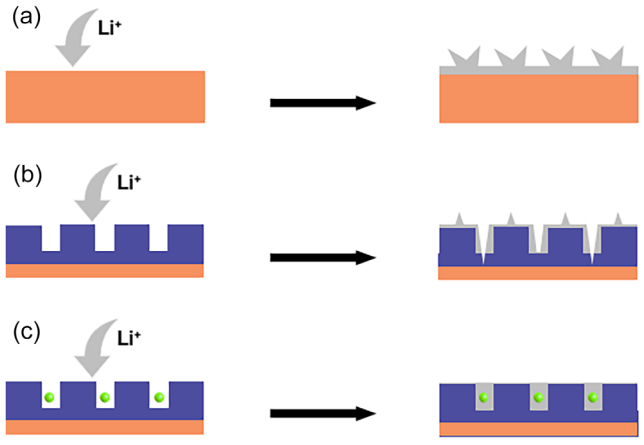

FIGURE 1 | Schematic representation of the lithium plating mechanism on the three different substrates involved: (a) Cu (in orange), (b) MX (in blue), and (c) Sn@MX (with the Sn-containing species in green and the MXene layers in blue).

25666223, 2026, 9, Downloaded from https://chemistry-europe.onlinelibrary.wiley.com/doi/10.1002/batt.70466 by Politecnico Di Torino Sist. Bibl Del Polit Di Torino, Wiley Online Library on [29/10/2026]. See the Terms and Conditions (https://onlinelibrary.wiley.com/terms-and-conditions) on Wiley Online Library for rules of use; OA articles are governed by the applicable Creative Commons License

spacing, while ^{119}Sn Mössbauer spectroscopy showed that tin is initially present primarily as SnO_2. Before cycling, an electrochemical reduction step against Li was applied to activate the SnO_2-containing composite and promote the formation of reduced Sn-based lithiophilic species. On the basis of the well-established electrochemical behavior of SnO_2-based electrodes [67] and of our previous direct investigation of closely related Sn/Ti oxide-MAX phase nanocomposites [68], this activation step is expected to promote the conversion of SnO_2 into reduced Sn species and, at sufficiently low potential, the formation of Li–Sn alloy phases. These Sn-derived species are therefore proposed to act as lithiophilic sites within the composite electrode. Electrochemical performance was evaluated by comparing Sn@MX with bare Cu and pristine MXene (MX) using a plating-stripping protocol based on the reservoir method [69], with an initial deposition at 2 mAh cm^{-2} followed by cycling at 1 mAh cm^{-2}. Under these conditions, Cu showed rapid consumption of the predeposited reservoir within the first 10 cycles, whereas MX lasted longer but reached depletion after ca. 50 cycles. In contrast, Sn@MX operated for more than 120 cycles, demonstrating its potential as an effective Li host. Furthermore, ex situ and operando optical microscopy revealed distinctly different Li nucleation behaviors on various substrates, confirming the advantages of Sn@MX.

2 | Results and Discussion

2.1 | Synthesis and Characterization

The Sn@MX composite was prepared through a two-step synthesis, as illustrated in Figure 2a. First, the MXene lamellae were expanded using cetyltrimethylammonium bromide (CTAB) in water; subsequently, $SnCl_4$ was added to the previous mixture to introduce Sn-containing species into the MXene-based composite. The successful modification of the MXene structure was investigated by XRD and ^{119}Sn Mössbauer spectroscopy.

The XRD patterns of the pristine MXene, the MXene expanded with CTAB (MX + CTAB), and the final Sn@MX product are reported in Figure 2b. The *00l* reflections shift to lower angles after CTAB treatment, specifically from 9.17°, 18.56°, and 28.07°, to 8.90°, 18.19°, and 27.21°, respectively (Figure 2c). This shift indicates an increase in the interlayer distance, confirming the expansion of the MXene interlayer spacing induced by CTAB. After the addition of $SnCl_4$, no significant shift of the 00l reflections is observed compared with MX + CTAB, suggesting that the incorporation of Sn-containing species does not further modify the expanded lamellar structure [70, 71].

The appearance of a new broad peak around 27° in Figure 2c can be attributed to cassiterite-phase SnO_2, indicating the expected formation of tin oxide species during the reaction of $SnCl_4$ in the aqueous environment [72]. The presence of SnO_2 was further confirmed by ^{119}Sn Mössbauer spectroscopy, as the Sn@MX spectrum (Figure 2d) shows exclusively the contribution of Sn(IV) oxide in the form of cassiterite, with an isomer shift (IS) of 0.02 mm s^{-1} [73].

The nominal amount of tin introduced during synthesis can be estimated from the precursor ratio. In the Sn@MX preparation, 155 mg of $SnCl_4$ were added to 350 mg of MXene, corresponding to 0.60 mmol of Sn, i.e., ca. 70 mg of Sn or ca. 90 mg of SnO_2. This corresponds to a nominal SnO_2/MXene mass ratio of approximately 0.26, or to a nominal SnO_2 fraction of ca. 20 wt% in the SnO_2/MXene composite, assuming the quantitative retention of tin during synthesis and subsequent washing. This value should therefore be considered as a nominal loading rather than

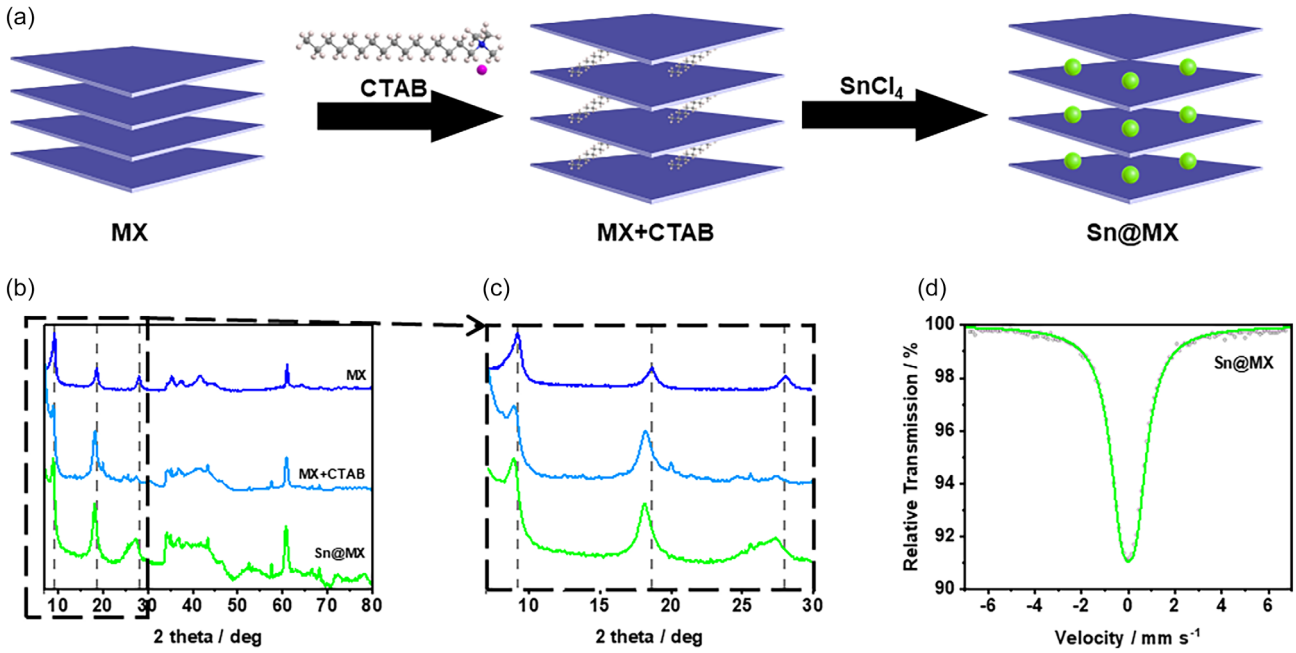

FIGURE 2 | (a) Schematic representation of the Sn@MX synthesis, with blue sheets representing the MXene lamellae and green spheres representing the Sn-containing species; (b) XRD pattern of the pristine MXene, MX + CTAB, and Sn@MX compounds, (c) with a zoom in the region between 7 and 30 deg; (d) ^{119}Sn Mössbauer spectrum of Sn@MX.

25666223, 2026, 9, Downloaded from https://chemistry-europe.onlinelibrary.wiley.com/doi/10.1002/batt.70466 by Politecnico Di Torino Sist. Bibl Del Polit Di Torino, Wiley Online Library on [29/10/2026]. See the Terms and Conditions (https://onlinelibrary.wiley.com/terms-and-conditions) on Wiley Online Library for rules of use; OA articles are governed by the applicable Creative Commons License

as an experimentally determined Sn content, as XRD and ^{119}Sn Mössbauer spectroscopy provide evidence for the formation of SnO_2, but they do not directly quantify the absolute Sn content or its local spatial distribution.

To further confirm the successful synthesis of the composite, Raman spectroscopy and scanning electron microscopy–energy-dispersive X-ray spectroscopy (SEM-EDX) analyses were carried out. In the Raman spectra reported in Figure S1, after CTAB addition, the vibrational mode located at approximately 210 cm^{-1}, commonly associated with out-of-plane Ti-C-T_x lattice vibrations, exhibits a red shift. In contrast, the A_{1g}(C) mode centered around 720 cm^{-1} undergoes a blue shift. According to previous Raman studies on $Ti_3C_2T_x$ MXenes, the high-frequency A_{1g}(C) mode is particularly sensitive to interlayer interactions and stacking effects, shifting toward higher wavenumbers upon intercalation and expansion of the interlayer spacing [74, 75]. The simultaneous redshift of the low-frequency mode and blueshift of the A_{1g}(C) band therefore indicate a modification of the local bonding environment induced by CTAB intercalation and are consistent with the increase of the MXene interlayer distance observed by XRD.

SEM images show that the lamellar morphology of MXene is preserved after the complete synthesis process, indicating that the layered structure remains intact (Figure S2). Furthermore, the successful incorporation of tin-containing species is confirmed by EDX analysis: the elemental mapping, reported in Figure S3, reveals a homogeneous distribution of Sn throughout the MXene matrix and yields an estimated Sn/Ti atomic ratio of 0.10, which is in good agreement with the theoretical value calculated from the precursor ratio.

2.2 | Electrochemical Test

To verify the benefits of the Sn@MX substrate on the lithium stripping-plating process, its electrochemical properties were studied and compared with bare Cu and pristine MX on Cu (MX). Galvanostatic tests were conducted in three-electrode Swagelok cells using metallic lithium as both counter and reference electrode, with 1 M lithium bis(trifluoromethanesulfonyl)imide (LiTFSI) in 1,3-dioxolane:1,2-dimethoxyethane (DOL:DME 1:1 v/v) containing 2 wt% $LiNO_3$ as electrolyte. The stripping-plating protocol was the following: (i) an initial slow reduction with a current density of 0.02 mA cm^{-2} was applied to electrochemically activate the SnO_2^- containing composite, in order to promote the conversion of SnO_2 into reduced electrochemically active Sn species with a lithiophilic character [68, 76]; (ii) 5 cycles of plating-stripping for 5 mAh cm^{-2} (5 h, 1 mA cm^{-2}) per cycle to stabilize the interface; (iii) deposition of a lithium reservoir [69] of 2 mAh cm^{-2}; and (iv) subsequent cycles at 1 mAh cm^{-2} and 1 mA cm^{-2}. To further investigate the interface evolution, after each 5 stripping-plating cycles, electrochemical impedance spectroscopy (EIS) was performed.

Although this initial reduction step is primarily required for Sn@MX, the same protocol was applied to Cu and MX to ensure a consistent electrochemical history and to minimize the impact of irreversible reactions during subsequent cycling, such as SEI formation and the reduction of surface oxide layers. In traditional LMBs with a lithiated cathode, the role of the lithium reservoir is to compensate for the plating irreversibility caused by the continuous electrolyte reduction required to repair the SEI damaged during stripping. Therefore, the larger this lithium excess, the longer the interfacial stability is maintained. In the case of batteries with nonlithiated cathodes (Li—S or Li–air), this initial amount of lithium determines the effective capacity of the negative electrode. In this work, reservoir depletion is therefore used as an operational electrochemical descriptor. It refers to the point at which the remaining electrochemically accessible Li reservoir is no longer sufficient to sustain stable stripping/plating under the imposed cycling conditions, as reflected by the rapid increase in stripping overpotential. This approach does not provide a direct quantitative separation between reversible Li and inactive or "dead" Li, which would require dedicated postmortem quantification methods.

The galvanostatic profiles of the three investigated substrates as working electrodes are shown in Figure 3. For greater clarity, the profiles presented here start from the first cycle at 1 mAh cm^{-2}, following the deposition of the lithium reservoir. The full tests—including the initial stabilization cycles and the counter electrode profile—are reported in the Supporting Information (Figures S4 and S5). When Cu is used as the substrate (Figure 3a,b,d), it shows a rapid and large increase in the stripping overpotential after the first few cycles, indicating that the lithium reservoir is rapidly exhausted. This demonstrates its limited ability to sustain reversible and stable lithium stripping-plating cycles [24]. During the initial stripping/plating cycles, the overpotential of the MX electrode is similar to that of copper in absolute value (Figure 3a); however, the electrode takes significantly longer to deplete the lithium reservoir (Figure 3b,e), thus exhibiting more stable cycling and lower irreversibility. After the first 20 h (10 cycles), a steady increase in overpotential is observed, and after 50 h (25 cycles), the overpotential behavior becomes markedly asymmetrical. This behavior is consistent with a progressive loss of electrochemically accessible lithium from the reservoir, likely associated with irreversible Li consumption and the formation of inactive or "dead" Li during repeated stripping/plating. However, the voltage profile alone does not allow the amount of "dead" Li to be quantitatively separated from the remaining reversible Li. Finally, after roughly 100 h (50 cycles), the stripping overpotential reaches the value of 0.5 V at which point the lithium reservoir can be considered depleted.

In the case of the Sn@MX substrate (Figure 3a), the initial overpotential is larger, due to the slower Li plating/stripping kinetics of the composite electrode. Moreover, the initial Sn@MX profiles appear more unstable than those of the other electrodes. In fact, at the 4th cycle, the nucleation overpotential increases significantly compared to previous cycles, then decreases from the 5th cycle onwards and stabilizes. However, this substrate was able to reach over 120 cycles without showing the electrochemical signatures of reservoir depletion observed for Cu and MX, as indicated by the much more stable stripping overpotential.

This highlights the beneficial role of electrochemically activated Sn-based lithiophilic species as preferential nucleation sites for lithium (Figure 3b,c). The final failure of the cell (Figure 3c) is likely attributable to a short circuit caused by irregular lithium growth after prolonged cycles. During the final cycles before

25666223, 2026, 9, Downloaded from https://chemistry-europe.onlinelibrary.wiley.com/doi/10.1002/batt.70466 by Politecnico Di Torino Sist. Bibl Del Polit Di Torino, Wiley Online Library on [29/10/2026]. See the Terms and Conditions (https://onlinelibrary.wiley.com/terms-and-conditions) on Wiley Online Library for rules of use; OA articles are governed by the applicable Creative Commons License

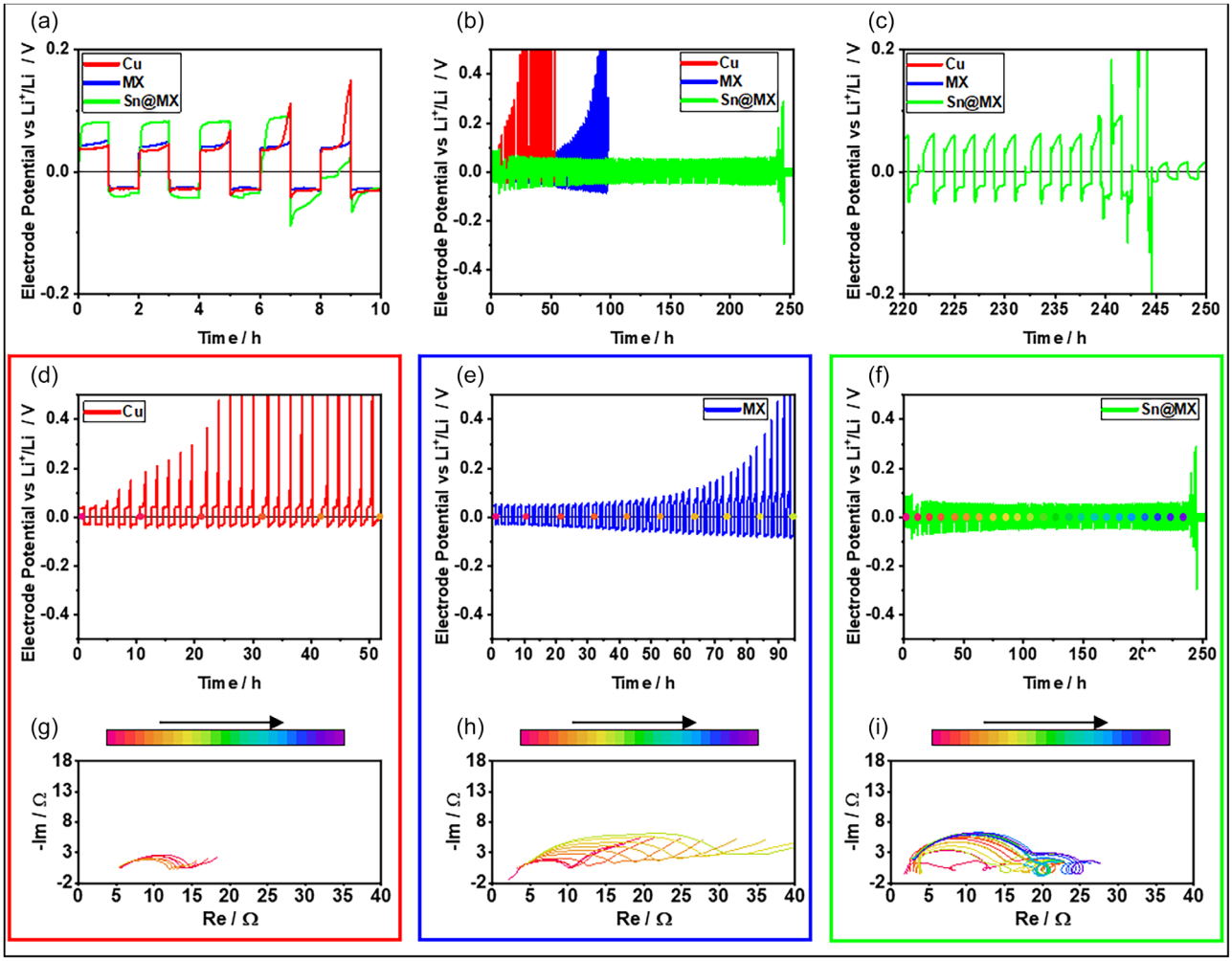

FIGURE 3 | Voltage profiles at 1 mAh cm^{-2} and EIS spectra. Above panel: comparison of the voltage profiles of the three substrates in the first 10 h (**3a**), whole time range (**3b**), and final 30 h (**3c**). Middle panel: voltage profiles of Cu (**3d**), MX (**3e**), and Sn@MX (**3f**). Lower panel: Nyquist plots of Cu (**3g**), MX (**3h**), and Sn@MX (**3i**) obtained after every 5 cycles of stripping-plating at the end of the plating. The colored markers in panels (a–f) indicate the type of studied material (red: Cu, blue: MX, green: Sn@MX), whereas those in panels (g–i) change progressively from red to violet with increasing cycling time, as indicated by the arrows above the graphs.

failure, indeed, the overpotential rapidly increases until it collapses to a value even lower than the initial one. This can be related to the formation of dendrites, which lead to local short-circuits and, therefore, to potential drops. Thus, although Sn@MX substantially improves the reversibility of Li plating/stripping and delays the depletion of the lithium reservoir, prolonged cycling can still lead to irregular lithium accumulation and eventually to cell failure.

It should be noted that the polarization observed during Li plating/stripping is not governed only by the intrinsic electronic conductivity of the substrate. Although Cu, MXene, and reduced Sn-based species are electronically conductive, the overall overpotential also depends on the Li nucleation barrier, the local Li^+ flux, SEI formation and rupture, ion transport through the porous electrode/electrolyte interface, and the evolving morphology and surface area of the Li deposit. Thus, the high electronic conductivity of Cu does not prevent large polarization when Li growth is heterogeneous and dendritic [6]. Similarly, the conductivity of pristine MXene is not sufficient to avoid progressive interfacial impedance growth if Li deposition remains partially surface-confined and inhomogeneous. In Sn@MX, the initially higher polarization can be attributed to the activation of SnO_2-containing species and to the formation of a complex interphase, possibly including electronically insulating Li_2O, before the beneficial effect of Sn-derived lithiophilic sites becomes dominant during prolonged cycling.

To better understand the overpotential evolution during stripping/plating processes, EIS spectra were acquired after every five stripping/plating cycles, at the end of the plating step, to provide insight into the interfacial kinetics of the Li^+/Li system. Due to the complexity of the analysis of the Li metal/electrolyte interface (see, for example, reference [77]) and to the use of Swagelok-type cells, which are not optimal for quantitative EIS measurements [78], the spectra are discussed only qualitatively. In particular, the overlapping contributions of SEI/interphase resistance, charge–transfer resistance, mass transport, evolving Li surface area, and porous-electrode effects prevent an unambiguous deconvolution of the different polarization processes. For this reason, neither equivalent-circuit fitting nor Distribution of Relaxation Times analysis was used to assign individual resistive contributions.

25666223, 2026, 9, Downloaded from https://chemistry-europe.onlinelibrary.wiley.com/doi/10.1002/batt.70466 by Politecnico Di Torino Sist. Bibl Del Polit Di Torino, Wiley Online Library on [29/10/2026]. See the Terms and Conditions (https://onlinelibrary.wiley.com/terms-and-conditions) on Wiley Online Library for rules of use; OA articles are governed by the applicable Creative Commons License

Nevertheless, state-of-the-art characterization studies of the Li^+/Li interface have shown that the charge transfer contribution can be relatively small compared with the overall impedance, and may therefore be negligible in DME-based electrolytes [79]. Similarly, the low-frequency diffusion contribution is known to remain limited in comparable systems, so that the impedance response is often largely governed by the SEI/interphase contribution [76]. In this framework, these EIS data should not be interpreted as a quantitative separation of the different interfacial processes, but rather as comparative fingerprints of the global interfacial evolution of the three electrodes during cycling.

The cell containing only copper (Figure 3g) exhibits, in the first cycle, a depressed semicircle followed at low frequency by a diffusion-related contribution, as commonly observed for Li/electrolyte interfaces [80]. This shape is often associated with the presence of a SEI [77]. The impedance then progressively decreases over time during the first 50 h (25 cycles). Therefore, in this case, the expansion of the surface area caused by uncontrolled dendrite growth is the predominant factor.

Both the MXene-modified substrates (Figure 3h,i) show a different diffusion behavior, stemming from the different nature of the interface. When using the bare MXene substrate (Figure 3h), the apparent interfacial impedance is initially similar to that of Cu, in agreement with the overpotential profile in Figure 3a; nonetheless, the temporal evolution differs as the resistance tends to increase rather than decrease, tripling (from approximately 10 to 30 Ω) after 100 h (50 cycles). In this case, the increase in apparent interfacial impedance suggests that interphase growth and/or transport limitations progressively become more significant than the increase in active surface area.

Finally, in the case of the Sn@MX sample (Figure 3i), the initial impedance is slightly higher (again, in agreement with Figure 3a) and then increases more slowly during the first 200 h (100 cycles), eventually stabilizing at approximately 25 Ω. The higher initial resistance of Sn@MX may be related to the formation of electronically insulating Li_2O during the electrochemical conversion of SnO_2 into reduced Sn species. Such a conversion is part of the electrochemical activation of SnO_2-based electrodes and may be followed, at low potential, by Li—Sn alloy formation. The appearance of a small inductive loop may reflect additional relaxation processes associated with the complex porous/interfacial structure of the Sn@MX electrode. However, this feature cannot be unambiguously assigned from the present measurements and is therefore not used for quantitative interpretation, even though it remains consistent with a more distributed lithium metal growth within the composite electrode rather than exclusively on the outer surface.

In addition, gas chromatography–mass spectrometry (GC–MS) analyses were carried out on the electrolyte recovered from the cycled cell to assess whether any specific degradation phenomena of the electrolyte could interfere with the behavior of the three studied substrates. The acquired chromatogram and mass spectra are reported in Figure S6. For all three cycled cells, the chromatograms remain comparable to that of the pristine electrolyte, and the detected species were assigned to the pristine electrolyte components and to the eluent. These results suggest that no significant amounts of soluble degradation products are formed under the investigated conditions. Therefore, the different electrochemical behaviors of the three electrodes are more likely associated with the nature of the substrates than with any markedly different electrolyte decomposition pathways.

The improved behavior of Sn@MX is likely related not only to the presence of Sn-derived lithiophilic sites, but also to their integration within a conductive and mechanically accommodating MXene-based scaffold. In this respect, the CTAB-induced expansion of the MXene lamellae is expected to play a role beyond facilitating the introduction of Sn-containing species, by increasing the accessible interlayer/porous volume, favoring electrolyte penetration, and providing internal space for Li deposition. The porous MXene architecture can therefore assist in buffering the volume changes associated with the initial SnO_2 reduction and subsequent Li—Sn alloy formation [81, 82], while the high electronic conductivity of $Ti_3C_2T_x$ promotes a more homogeneous electron distribution throughout the composite electrode. However, because a Sn-free expanded MXene control was not electrochemically tested, the individual contribution of the expanded interlayer spacing cannot be fully decoupled from that of the Sn-derived lithiophilic sites. The comparison between pristine MXene and Sn@MX nevertheless indicates that the MXene scaffold alone is insufficient to fully control Li growth, whereas the combination of lithiophilic Sn-derived species, electronic connectivity, and structural accommodation explains the enhanced reversibility of Li plating/stripping compared to both bare Cu and pristine MXene [83, 84].

In conclusion, the electrochemical characterizations demonstrate that the introduction of Sn-containing lithiophilic species within the porous lamellar architecture of MXene-based electrodes results in a substrate capable of accommodating metallic lithium for more than 120 cycles. This approach delays the electrochemical signature of irreversible loss of active lithium, which is commonly associated with inactive or "dead" Li formation during repeated stripping/plating.

2.3 | Optical Microscopy

Because of the high reactivity of metallic lithium, post mortem morphology analysis is particularly sensitive to artifacts arising from cell opening, separator removal, and sample transfer. In the present work, ex situ optical microscopy was therefore used as a qualitative tool to compare the macroscopic and mesoscale morphology of the cycled electrodes, while operando optical microscopy was used to follow Li growth directly during plating in a cross-sectional configuration. These observations will enable the comparison of the spatial distribution and growth behavior of Li deposits on the different substrates, providing a qualitative comparison of Li growth under ex situ and operando optical conditions.

Pristine copper (Figure 4a,c,e) displays a typical morphology with evident roughness resulting from the industrial lamination process of the foil. In contrast, the electrodes coated with MXene (Figure 4g,i,k) and with Sn-modified MXene (Figure 4m,o,q) exhibit the characteristic globular morphology typical of battery electrodes composed of active material, organic binder, and conductive carbon. Following the final plating cycle shown in

25666223, 2026, 9, Downloaded from https://chemistry-europe.onlinelibrary.wiley.com/doi/10.1002/batt.70466 by Politecnico Di Torino Sist. Bibl Del Polit Di Torino, Wiley Online Library on [29/10/2026]. See the Terms and Conditions (https://onlinelibrary.wiley.com/terms-and-conditions) on Wiley Online Library for rules of use; OA articles are governed by the applicable Creative Commons License

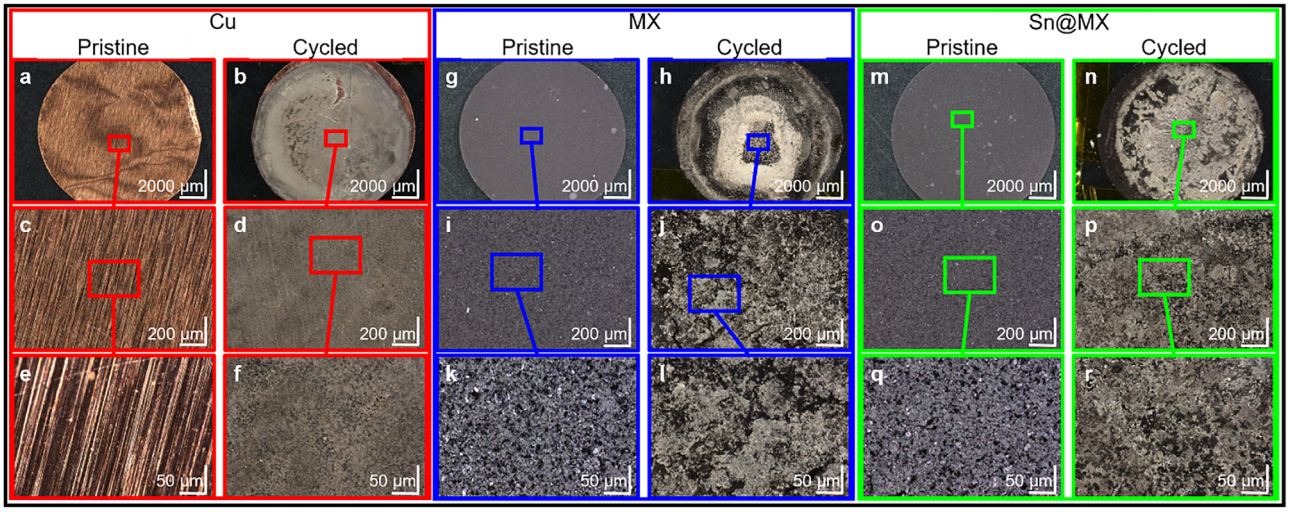

FIGURE 4 | Optical microscopy images of pristine and cycled electrodes acquired at different magnifications: 20× (a,b,g,h,m,n), 200× (c,d,i,j,o,p), and 500× (e,f,k,l,q,r).

Figure 3, the lithium deposits exhibit significantly different morphologies depending on the substrate used. In the case of bare Cu (Figure 4b,d,f), the lithium layer appears macroscopically homogeneous. In contrast, for the MXene-based electrodes—specifically for Sn@MX (Figure 4n,p,r) and even more so for pristine MXene (Figure 4h,j,l)—the deposit appears nonuniform, with areas of varying density and some uncovered regions. Beyond the separator removal procedure, which may mechanically damage the deposited lithium layer, these differences are attributable to the porosity of the composite electrodes, which allows the lithium to grow within the electrode cavities. The differing lifespans of the electrodes must also be considered, as the composites (specifically Sn@MX) operated for significantly longer than bare Cu. Nonetheless, the presence of Sn-derived lithiophilic sites appears to promote a more homogeneous dispersion of metallic lithium on the electrode surface compared to the case with MXene alone.

It should be emphasized that these optical microscopy observations provide morphological evidence of different Li deposition behaviors, but they cannot be used to quantitatively determine the amount of inactive or "dead" Li. They are therefore used here as a qualitative postmortem comparison of the cycled electrodes.

To better understand these aspects, operando optical microscopy measurements were carried out during lithium growth (first plating process), observing the system in cross-section rather than from a top-view perspective. To achieve this, the substrates were cycled against lithium in an optical cell equipped with a glass window, acquiring images during the galvanostatic test. Lithium plating was performed by applying current densities of 1 and 0.1 mA cm^{-2}. Figure 5 reports the images acquired at the beginning of the plating (Figure 5a,d,g), after 5 min (Figure 5b,e,h), and after 10 min (Figure 5c,f,i) for the different substrates at 1 mA cm^{-2}.

On Cu (Figure 5a–c), the lithium tends to grow, as expected, in a dendritic manner [24], due to the low lithiophilicity of the substrate and the resulting inhomogeneous Li^+ concentration gradients. With the MX electrode (Figure 5d–f), the tendency toward dendritic growth is mitigated, as evidenced by the reduced length and lower density of Li dendrites. However, after only 5 min, the onset of significant surface plating is observed, with lithium beginning to deposit on the outer surface rather than within the electrode structure. This suggests that the MX electrode architecture alone is insufficient to effectively confine lithium growth within the electrode pores. In contrast, when Sn@MX is used (Figure 5g–i), lithium tends to deposit inside the electrode structure, preferentially filling the porous network rather than nucleating on the surface. This results in a thinner and more homogeneous lithium deposit on the substrate, supporting the trends previously observed in the electrochemical profiles.

The observed growth mechanism could be influenced by the cell geometry and assembly, which may involve the formation of electrolyte bubbles and, most importantly, by the applied current. To further assess the influence of current density on the early Li deposition behavior, additional operando optical microscopy tests were performed on MX and Sn@MX at 0.1 mA cm^{-2}, i.e., 10 times lower than the current density used in the previous experiment. These low-current measurements were intended to decouple, at least qualitatively, the intrinsic effect of the substrate from the exacerbated dendritic growth promoted by high current density.

At this lower current density, Li deposition on MX (Figure 5j–l) is more readily accommodated within the electrode structure than at 1 mA cm^{-2}, confirming that dendritic/surface growth is promoted under harsher current conditions. Nevertheless, the lithium deposit remains spatially inhomogeneous, with localized dense regions. By contrast, Sn@MX (Figure 5m–o) shows a more uniform filling of the porous electrode structure, indicating that the Sn-derived lithiophilic sites help distribute Li nucleation and growth even when the kinetic driving force is reduced. This comparison supports the conclusion that the improvement provided by Sn@MX over pristine MXene is not only a high-current effect, but is also linked to the modified lithiophilicity of the substrate.

25666223, 2026, 9, Downloaded from https://chemistry-europe.onlinelibrary.wiley.com/doi/10.1002/batt.70466 by Politecnico Di Torino Sist. Bibl Del Polit Di Torino, Wiley Online Library on [29/10/2026]. See the Terms and Conditions (https://onlinelibrary.wiley.com/terms-and-conditions) on Wiley Online Library for rules of use; OA articles are governed by the applicable Creative Commons License

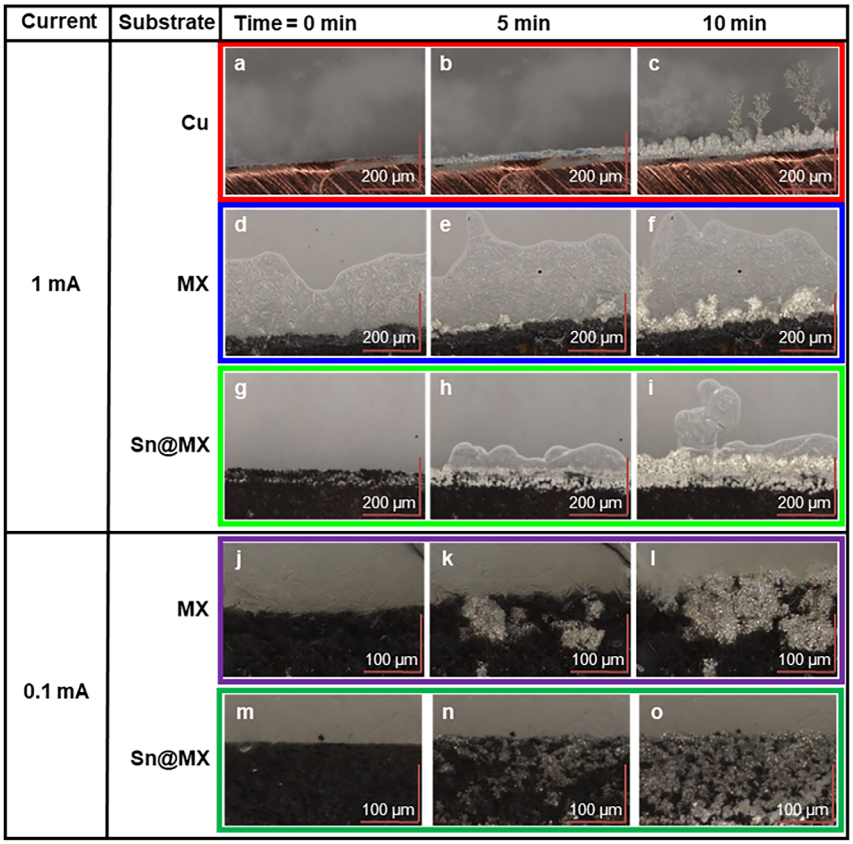

FIGURE 5 | Optical microscope images at 200× magnification acquired during the first lithium plating process. Upper panel: images of Cu (a–c), MX (d–f), and Sn@MX (g–i) electrodes, at 1 mA cm^{-2} and at the beginning (a,d,g), after 5 min (b,e,h), and after 10 min (c,f,i). Lower panel: images of MX (j,k,l) and Sn@MX (m,n,o) electrodes at 0.1 mA cm^{-2}: at the beginning (j,m), after 10 min (k,n), and after 20 min (l,o).

Overall, these operando observations support the conclusion that Sn@MX modifies the Li growth behavior compared with pristine MXene, promoting a more spatially distributed deposition within the porous electrode structure.

3 | Conclusion

A Sn-modified $Ti_3C_2T_x$ MXene composite electrode (Sn@MX) was investigated as a host for lithium metal anodes, combining the lamellar architecture of MXene with Sn-derived lithiophilic sites to regulate Li deposition. Structural analyses confirmed the expansion of the MXene interlayer spacing and showed that Sn is initially present as SnO_2 within the composite electrode. After electrochemical activation against Li, the resulting Sn-based lithiophilic sites promote a more homogeneous and spatially distributed Li deposition. Electrochemical characterization revealed that Sn@MX maintains stable plating-stripping for over 120 cycles, significantly outperforming both bare Cu and pristine MXene substrates. Ex situ and operando optical microscopy further support the role of Sn@MX in promoting homogeneous Li deposition within the electrode structure and mitigating dendritic growth. These results underscore the importance of combining porous lamellar architectures with lithiophilic sites to delay lithium reservoir depletion and improve the reversibility of lithium metal anodes. More broadly, this study establishes a rational design strategy for high-performance Li hosts, advancing the development of practical lithium metal batteries for high-energy storage applications.

4 | Methods

4.1 | Synthesis of $Ti_3C_2T_x$ MXene

$Ti_3C_2T_x$ MXenes were produced by etching commercial Ti_3AlC_2 MAX-phase (Sigma-Aldrich) in a polytetrafluoroethylene (PTFE) beaker, using 20 mL of a 30 wt% hydrofluoric acid (HF) aqueous solution per gram of MAX-phase processed. The powder was slowly added to the reaction solution over 5 min, as the reaction between HF and the MAX phase causes significant hydrogen gas evolution. The dispersion was stirred at room temperature for 5 h. Afterwards, the sample was centrifuged for 15 min at 5000 rpm to separate the precipitate from the supernatant. It was then washed with Milli-Q water and centrifuged 5–6 times until the solution's pH reached 6. The powder was finally dried under vacuum at 80 °C overnight.

4.2 | Synthesis of Sn@MX

350 mg of $Ti_3C_2T_x$ were first stirred for 24 h at 40 °C in 60 mL of 0.25 wt% CTAB water solution. Then, 155 mg of $SnCl_4$ (Sigma-Aldrich, 98%) were added and stirred for 12 h. This precursor ratio corresponds to a nominal SnO_2/MXene mass ratio of

25666223, 2026, 9, Downloaded from https://chemistry-europe.onlinelibrary.wiley.com/doi/10.1002/batt.70466 by Politecnico Di Torino Sist. Bibl Del Polit Di Torino, Wiley Online Library on [29/10/2026]. See the Terms and Conditions (https://onlinelibrary.wiley.com/terms-and-conditions) on Wiley Online Library for rules of use; OA articles are governed by the applicable Creative Commons License

ca. 0.26, assuming complete hydrolysis of $SnCl_4$ to SnO_2 and quantitative retention of tin in the recovered solid. The solution was centrifuged for 15 min at 5000 rpm to recover the product and then washed with deionised water and dried overnight at 70 °C.

4.3 | X-Ray Diffraction

The XRD patterns were collected using a PANalytical X'Pert Pro MPD diffractometer with a copper source (Kα = 1.5418 Å) in the range 7°–80° with a step size of 0.02°.

4.4 | Mössbauer Spectroscopy

^{119}Sn Mössbauer spectra were collected in constant acceleration mode at room temperature, using $Ca^{119m}SnO_3$ as the source and a LiF scintillation detector for γ-rays. The velocity scale was calibrated with a high-purity α-Fe foil at room temperature using a ^{57}Co:Rh source. The isomer shifts are referenced to the $CaSnO_3$ source. The spectra were analyzed using a standard least-squares fitting procedure with Lorentzian quadrupole doublets. This method allowed the determination of hyperfine parameters such as isomer shift (δ), quadrupole splitting (Δ), full linewidth at half-maximum (Γ), and the relative resonance areas of different spectral components.

4.5 | Raman Spectroscopy

Micro-Raman measurements were carried out on a confocal labRAM (Horiba Jobin-Yvon) spectrometer operating in back-scattering configuration. The scattered light was detected by a charge-coupled device (CCD-Sincerity, Jobin-Yvon). A microscope (Olympus BX40) was used both to focus the excitation on the samples and to collect the scattered light. To avoid sample degradation, a solid-state laser at 785 nm, with a long working distance of 50× objective and attenuated power to 1 mW, was used. The spectra were collected in the range of 100–800 cm^{-1}, with a grating of 1200 lines mm^{-1}, and slit and hole of 100 and 300 μm, respectively.

4.6 | SEM and EDX

SEM images and EDX elemental maps were acquired using a JEOL JSM-IT200 scanning electron microscope operated at 15 kV.

4.7 | Electrode Preparation

For Cu, bare copper foil (MTI, thickness 9 μm) was used directly as the electrode. For MX and Sn@MX, the electrodes were fabricated by mixing, respectively, the powders with Super P carbon and a 5 wt% solution of poly(vinylidene fluoride) (PVdF) in NMP, with a weight ratio of 80:10:10, using a Kurabo KK-300SS mixer at 1000 rpm for 5 min and then 1500 rpm for 5 min until obtaining a homogeneous ink. NMP was added up to a solvent-to-slurry mass ratio of 70% to achieve the ideal slurry density. The slurry was then tape-casted onto copper foils (MTI, thickness 9 μm) with a doctor blade to obtain a wet thickness of 200 μm. The films were dried in vacuo at 120 °C for 12 h and subsequently calendared.

4.8 | Electrochemical Measurements

The electrochemical performance of the materials was evaluated in three-electrode Swagelok-type cells. The cells were prepared in an argon-filled glovebox (MBraun). The working electrodes were cut into 12-mm diameter disks, while the reference and counter electrodes were lithium metal disks with the same diameter (12 mm). The electrolyte was 20 μL of 1 M LiTFSI (Sigma-Aldrich, 99.99%) in DOL (Sigma-Aldrich, anhydrous, 99.8%) to DME (Sigma-Aldrich, anhydrous, 99.5%) in a 1:1 volume ratio with 2 wt% $LiNO_3$ (Sigma-Aldrich, 99.99%) with Celgard 2325 as separator. The cells were cycled using the Biologic VSP potentiostat at 25 °C with the following protocol: a first reduction to 0.01 V at 0.02 mA cm^{-2}; 5 cycles of plating-stripping at 5 mAh cm^{-2} (5 h for each step at 1 mA cm^{-2}), using −1.0 and 1.0 V as cutoff if necessary, respectively; 1 cycle of plating at 2 mAh cm^{-2} (2 h at 1 mA cm^{-2}), using −1.0 V as cutoff if necessary; subsequent cycles of stripping-plating at 1 mAh cm^{-2} (1 h for each step at 1 mA cm^{-2}), using 1.0 and −1.0 V as cutoff if necessary.

4.9 | Optical Microscope

The optical images were acquired using a Leica Microsystems DM2700 M upright materials microscope equipped with a digital camera and operated via Leica Application Suite software. For the ex situ images, the electrodes were recovered from the cell and placed between two microscope slides sealed in an argon-filled glovebox (MBraun). For the *operando* measurements, an EL-CELL ECC-Opto-10 was used in a side-by-side electrode setup, cycled at 25 °C using a Biologic SP-50e potentiostat.

4.10 | GC–MS

The electrolyte of cycled cells was recovered from the Celgard separator by using acetonitrile, which was also chosen as eluent for the GC–MS experiment. For the analysis, a Shimadzu GCMS QP-2010 Plus apparatus was used. The column was heated up to 250 °C, and then the species were injected with a split ratio equal to 10. The MS stage was switched off between 2.15 and 3.00 min during the elution of the very intense acetonitrile peak.

Acknowledgments

M. T. Sougrati is gratefully acknowledged for technical help in the collection of the ^{119}Sn Mössbauer spectra. L.S. gratefully acknowledges ANR for funding through the project Labex STORE-EX (Grant ANR-10-LABX-76-01). This work was financed by the Research Fund for the Italian Electrical System under the Three-Year Research Plan 2025–2027 (MASE, Decree n.388 of November 6th, 2024), in compliance with the Decree of April 12th, 2024.

Open access publication funding provided by COUPERIN CY26.

25666223, 2026, 9, Downloaded from https://chemistry-europe.onlinelibrary.wiley.com/doi/10.1002/batt.70466 by Politecnico Di Torino Sist. Bibl Del Polit Di Torino, Wiley Online Library on [29/10/2026]. See the Terms and Conditions (https://onlinelibrary.wiley.com/terms-and-conditions) on Wiley Online Library for rules of use; OA articles are governed by the applicable Creative Commons License

Funding

This work was supported by the Agence Nationale de la Recherche (ANR-10-LABX- 76-01), Research Fund for the Italian Electrical System (Three-Year Research Plan 2025-2027).

Conflicts of Interest

The authors declare no conflicts of interest.

Data Availability Statement

The data that support the findings of this study are available from the corresponding author upon reasonable request.

References

1. A. Nekahi, A. K. Madikere Raghunatha Reddy, X. Li, et al., "Rechargeable Batteries for the Electrification of Society: Past, Present, and Future," *Electrochemical Energy Reviews* 8 (2025): 1, https://doi.org/10.1007/s41918-024-00235-8.

2. H. Xiao, J. Zhao, Q. Gao, et al., "Recent Advances in Fast-Charging Lithium-Ion Batteries: Mechanism, Materials, and Future Opportunities," *Chemical Engineering Journal* 506 (2025): 159927, https://doi.org/10.1016/j.cej.2025.159927.

3. Y. Zhang, H. Wang, Z. Li, et al., "Innovative Anode Design to Enhance Both Volumetric and Gravimetric Energy Densities of $LiCoO_2$||Graphite Pouch Cells," *Advanced Energy Materials* 15 (2025): 2403804, https://doi.org/10.1002/aenm.202403804.

4. Y. Dong, C. Liu, M. Rui, et al., "Review on Graphite Anodes for Fast-Charging Lithium-Ion Batteries: Mechanism Modification and Characterizations," *Advanced Functional Materials* 35 (2025): 2506190, https://doi.org/10.1002/adfm.202506190.

5. S. Mao, Y. Wang, Y. Lu, et al., "In Situ Evaluation and Manipulation of Lithium Plating Morphology Enabling Safe and Long-Life Lithium-Ion Batteries," *InfoMat* 7 (2025): e12612, https://doi.org/10.1002/inf2.12612.

6. A. Mohammadi, L. Monconduit, L. Stievano, et al., "Measuring the Nucleation Overpotential in Lithium Metal Batteries: Never Forget the Counter Electrode!," *Journal of the Electrochemical Society* 169 (2022): 070509, https://doi.org/10.1149/1945-7111/ac7e73.

7. R. Younesi, G. M. Veith, P. Johansson, et al., "Lithium Salts for Advanced Lithium Batteries: Li-Metal, Li-O2, and Li-S," *Energy and Environmental Science* 8 (2015): 1905–1922, https://doi.org/10.1039/c5ee01215e.

8. P. Zou, Y. Sui, H. Zhan, et al., "Polymorph Evolution Mechanisms and Regulation Strategies of Lithium Metal Anode Under Multiphysical Fields," *Chemical Reviews* 121 (2021): 5986–6056, https://doi.org/10.1021/acs.chemrev.0c01100.

9. Q. Wang, B. Liu, Y. Shen, et al., "Confronting the Challenges in Lithium Anodes for Lithium Metal Batteries," *Advanced Science* 8 (2021): 2101111, https://doi.org/10.1002/advs.202101111.

10. S. Kim, G. Park, S. J. Lee, et al., "Lithium-Metal Batteries: From Fundamental Research to Industrialization," *Advanced Materials* 35 (2023): 2206625, https://doi.org/10.1002/adma.202206625.

11. Y. Xu, K. Dong, Y. Jie, et al., "Promoting Mechanistic Understanding of Lithium Deposition and Solid-Electrolyte Interphase (SEI) Formation Using Advanced Characterization and Simulation Methods: Recent Progress, Limitations, and Future Perspectives," *Advanced Energy Materials* 12 (2022): 2200398, https://doi.org/10.1002/aenm.202200398.

12. H. Chen, C.-J. Zhou, X.-R. Dong, et al., "Revealing the Superiority of Fast Ion Conductor in Composite Electrolyte for Dendrite-Free Lithium-Metal Batteries," *ACS Applied Materials and Interfaces* 13 (2021): 22978–22986, https://doi.org/10.1021/acsami.1c04115.

13. M. Tao, J. Chen, H. Lin, et al., "Recent Advances in Quantifying the Inactive Lithium and Failure Mechanism of Li Anodes in Rechargeable Lithium Metal Batteries," *Journal of Energy Chemistry* 96 (2024): 226–248, https://doi.org/10.1016/j.jechem.2024.04.030.

14. S. Li, W. Zhang, Q. Wu, et al., "Synergistic Dual-Additive Electrolyte Enables Practical Lithium-Metal Batteries," *Angewandte Chemie - International Edition* 59 (2020): 14935–14941, https://doi.org/10.1002/anie.202004853.

15. H. Du, Y. Wang, Y. Kang, et al., "Side Reactions/Changes in Lithium-Ion Batteries: Mechanisms and Strategies for Creating Safer and Better Batteries," *Advanced Materials* 36 (2024): 2401482, https://doi.org/10.1002/adma.202401482.

16. A. Mohammadi, P. Ghorbanzade, J. M. López del Amo, et al., "From Formation to Reactivation of Inactive Lithium in Lithium Metal Anodes," *ChemElectroChem* 12 (2025): e202500242, https://doi.org/10.1002/CELC.202500242.

17. S. Tang, Q. Wei, B. Liu, et al., "Simultaneous Manipulation of Electric Double Layer and Zn (100) Deposition Enabled by Anions for Highly Stable Zn Anodes," *Angewandte Chemie* 137 (2025): e202510252, https://doi.org/10.1002/ange.202510252.

18. G. M. Hobold, J. Lopez, R. Guo, et al., "Moving Beyond 99.9% Coulombic Efficiency for Lithium Anodes in Liquid Electrolytes," *Nature Energy* 6 (2021): 951–960, https://doi.org/10.1038/s41560-021-00910-w.

19. X. Sun, X. Zhang, Q. Ma, et al., "Revisiting the Electroplating Process for Lithium-Metal Anodes for Lithium-Metal Batteries," *Angewandte Chemie* 132 (2020): 6730–6739, https://doi.org/10.1002/ange.201912217.

20. H. Li, C. Hong, R. Tao, et al., "Hybrid Conductive-Lithophilic-Fluoride Triple Protection Interface Engineering: Dendrite-Free Reverse Lithium Deposition for High-Performance Lithium Metal Batteries," *Journal of Energy Chemistry* 101 (2025): 416–428, https://doi.org/10.1016/j.jechem.2024.10.002.

21. L. Zeng, L. Gao, T. Ou, et al., "A Fluorinated Bifunctional Additive Achieving Stable Electrode/Electrolyte Interfaces for High-Voltage Lithium-Metal Batteries," *Journal of Materials Chemistry A* 13 (2025): 12471–12481, https://doi.org/10.1039/d5ta00416k.

22. S. Liu, X. Ji, N. Piao, et al., "An Inorganic-Rich Solid Electrolyte Interphase for Advanced Lithium-Metal Batteries in Carbonate Electrolytes," *Angewandte Chemie - International Edition* 133 (2021): 3661–3671, https://doi.org/10.1002/anie.202012005.

23. C. Guo, Y. Guo, R. Tao, et al., "Uniform Lithiophilic Layers in 3D Current Collectors Enable Ultrastable Solid Electrolyte Interphase for High-Performance Lithium Metal Batteries," *Nano Energy* 96 (2022): 107121, https://doi.org/10.1016/j.nanoen.2022.107121.

24. Q. Li, S. Zhu, and Y. Lu, "3D Porous Cu Current Collector/Li-Metal Composite Anode for Stable Lithium-Metal Batteries," *Advanced Functional Materials* 27 (2017): 1606422, https://doi.org/10.1002/adfm.201606422.

25. J. Touja, N. Louvain, L. Stievano, et al., "An Overview on Protecting Metal Anodes With Alloy-Type Coating,"*Batteries and Supercaps* 4 (2021): 1252–1266, https://doi.org/10.1002/batt.202100009.

26. H. He, J. Shang, S. Li, et al., "Enabling Interfacially Compatible and High-Voltage-Tolerant Lithium Metal Batteries With Gradient Composited Solid-State Electrolytes," *Journal of Materials Chemistry A* 12 (2024): 22971–22980, https://doi.org/10.1039/d4ta03587a.

27. R. Che, S. Cheng, C. Huang, et al., "Poly(vinylidene Fluoride)-Based Janus Separators With an Ultrathin Conductive Layer for Suppressing Lithium Dendrite Growth," *Chemical Engineering Journal* 509 (2025): 161238, https://doi.org/10.1016/j.cej.2025.161238.

28. B. Yang, A. Hu, T. Li, et al., "Eliminating Water Hazards and Regulating Electrode-Electrolyte Interfaces by Multifunctional Sacrificial Electrolyte Additives for Long-Life Lithium Metal Batteries,"

25666223, 2026, 9, Downloaded from https://chemistry-europe.onlinelibrary.wiley.com/doi/10.1002/batt.70466 by Politecnico Di Torino Sist. Bibl Del Polit Di Torino, Wiley Online Library on [29/10/2026]. See the Terms and Conditions (https://onlinelibrary.wiley.com/terms-and-conditions) on Wiley Online Library for rules of use; OA articles are governed by the applicable Creative Commons License

Energy Storage Materials 70 (2024): 103512, https://doi.org/10.1016/j.ensm.2024.103512.

29. X. He, D. Bresser, S. Passerini, et al., "The Passivity of Lithium Electrodes in Liquid Electrolytes for Secondary Batteries," *Nature Reviews Materials* 6 (2021): 1036–1052, https://doi.org/10.1038/s41578-021-00345-5.

30. E. Carena, L. Mezzomo, N. Vallana, et al., "PVDF-HFP Based, Quasi-Solid Nanocomposite Electrolytes for Lithium Metal Batteries," *Small* 20 (2024): 2311805, https://doi.org/10.1002/smll.202311805.

31. N. Vallana, E. Carena, N. Ceribelli, et al., "Host-Guest Interactions and Transport Mechanism in Poly(vinylidene Fluoride)-Based Quasi-Solid Electrolytes for Lithium Metal Batteries," *ACS Applied Energy Materials* 7 (2024): 1606–1617, https://doi.org/10.1021/acsaem.3c03046.

32. L. Li, H. Dai, and C. Wang, "Electrolyte Additives: Adding the Stability of Lithium Metal Anodes," *Nano Select* 2 (2021): 16–36, https://doi.org/10.1002/nano.202000164.

33. N. Zhu, Y. Yang, Y. Li, et al., "Carbon-Based Interface Engineering and Architecture Design for High-Performance Lithium Metal Anodes," *Carbon Energy* 6 (2024): e423, https://doi.org/10.1002/cey2.423.

34. Z. Hao, Y. Lu, G. Yang, et al., "Designing Current Collectors to Stabilize Li Metal Anodes," *Advanced Materials* 37 (2025): 2415258, https://doi.org/10.1002/adma.202415258.

35. C. Sun, L. Gao, W. Rong, et al., "Lithium Directed Growth Triggered by Vertical Interface Activity Gradient Framework Enabling Long-Life Li Metal Anode," *Chemical Engineering Journal* 503 (2025): 158148, https://doi.org/10.1016/j.cej.2024.158148.

36. Y. Ding, N. Yi, F. Zhang, et al., "Recent Advances in 3D Cu Current Collectors for Li Metal Anodes," *Materials Science and Engineering: B* 321 (2025): 118459, https://doi.org/10.1016/j.mseb.2025.118459.

37. Y. Liu, Y. Zhai, Y. Xia, et al., "Recent Progress of Porous Materials in Lithium-Metal Batteries," *Small Structures* 2 (2021): 2000118, https://doi.org/10.1002/sstr.202000118.

38. H. Liu, J. Di, P. Wang, et al., "A Novel Design of 3D Carbon Host for Stable Lithium Metal Anode," *Carbon Energy* 4 (2022): 654–664, https://doi.org/10.1002/cey2.193.

39. J. Yun, E.-S. Won, H.-S. Shin, et al., "Efficient and Robust Lithium Metal Electrodes Enabled by Synergistic Surface Activation-Passivation of Copper Frameworks," *Journal of Materials Chemistry A* 7 (2019): 23208–23215, https://doi.org/10.1039/c9ta08779f.

40. Z. Zhu, B. Liu, Y. Qian, et al., "Spatially Distributed Lithiophilic Gradient in Low-Tortuosity 3D Hosts via Capillary Action for High-Performance Li Metal Anodes," *Advanced Energy Materials* 13 (2023): 2203687, https://doi.org/10.1002/aenm.202203687.

41. H.-J. Noh, M.-H. Lee, B. G. Kim, et al., "3D Carbon-Based Porous Anode With a Pore-Size Gradient for High-Performance Lithium Metal Batteries," *ACS Applied Materials and Interfaces* 13 (2021): 55227–55234, https://doi.org/10.1021/acsami.1c17616.

42. A. Mohammadi, A. Hagopian, S. Sayegh, et al., "Towards Understanding the Nucleation and Growth Mechanism of Li Dendrites on Zinc Oxide-Coated Nickel Electrodes," *Journal of Materials Chemistry A* 10 (2022): 17593–17602, https://doi.org/10.1039/d2ta04466h.

43. W. Huang, Y. Yu, Z. Hou, et al., "Dendrite-Free Lithium Electrode Enabled by Graphene Aerogels With Gradient Porosity," *Energy Storage Materials* 33 (2020): 329–335, https://doi.org/10.1016/j.ensm.2020.08.032.

44. M.-Qi Zhu, D.-Xu Ye, X.-Yi Teng, et al., "Selective Lithium Deposition Through 3D Copper Collector With Lithiophilic Alloy "Skins" and Curvature Boundaries for Dendrite-Free Lithium-Metal Anodes," *Rare Metals* 45 (2026): e70110, https://doi.org/10.1002/rar2.70110.

45. M. Naguib, V. N. Mochalin, M. W. Barsoum, et al., "25th Anniversary Article: MXenes: A New Family of Two-Dimensional Materials," *Advanced Materials* 26 (2014): 992–1005, https://doi.org/10.1002/adma.201304138.

46. M. Khazaei, A. Ranjbar, K. Esfarjani, et al., "Insights Into Exfoliation Possibility of MAX Phases to MXenes † propose 37 MAX Phases for Successful Exfoliation Into 2D Ti," *Physical Chemistry Chemical Physics* 20 (2018): 8579–8592, https://doi.org/10.1039/c7cp08645h.

47. M. Greaves, S. Barg, and M. A. Bissett, "MXene-Based Anodes for Metal-Ion Batteries," *Batteries and Supercaps* 3 (2020): 214–235, https://doi.org/10.1002/BATT.201900165.

48. A. Gentile, C. Ferrara, S. Tosoni, et al., "Enhanced Functional Properties of $Ti_3C_2T_x$ MXenes as Negative Electrodes in Sodium-Ion Batteries by Chemical Tuning," *Small Methods* 4 (2020): 2000314, https://doi.org/10.1002/smtd.202000314.

49. G. Behzadi pour and L. Fekri aval, "Recent Advances in Supercapacitors Based on MXene Surface Modification: A Review of Symmetric and Asymmetric Electrodes Material,"*Results in Engineering* 24 (2024): 103045, https://doi.org/10.1016/j.rineng.2024.103045.

50. S. Jayakumar, P. C. Santhosh, S. Ramakrishna, et al., "($Ti_3C_2T_x$) MXene: A Comprehensive Review of Advancements in Synthesis Protocols, Applications in Supercapacitors, Sustainability Targets and Future Prospects," *Journal of Energy Storage* 97 (2024): 112741, https://doi.org/10.1016/j.est.2024.112741.

51. P. Eghbali, A. Hassani, Sław Wacławek, et al., "Recent Advances in Design and Engineering of MXene-Based Catalysts for Photocatalysis and Persulfate-Based Advanced Oxidation Processes: A State-of-the-Art Review," *Chemical Engineering Journal* 480 (2024): 147920, https://doi.org/10.1016/j.cej.2023.147920.

52. T. R. Seling, M. Songsart-Power, A. K. Shringi, et al., "$Ti_3C_2T_x$ MXene-Based Hybrid Photocatalysts in Organic Dye Degradation: A Review," *Molecules* 30 (2025): 1463, https://doi.org/10.3390/molecules30071463.

53. N. Subha, L. R. Nagappagari, A. Ravi Sankar, et al., "A Review on Recent Advances in g-C_3N_4-MXene Nanocomposites for Photocatalytic Applications," *Nanotechnology* 35 (2024): 502002, https://doi.org/10.1088/1361-6528/ad7e2f.

54. A. Sreedhar and J. S. Noh, "Role of Emerging 2D Nb_2CT_x MXene for Multiple Toxic Matter Degradation, H_2 Generation, and H_2 Storage Applications: A Review," *Journal of Water Process Engineering* 75 (2025): 107996, https://doi.org/10.1016/j.jwpe.2025.107996.

55. L. Biswal, R. Mohanty, S. Nayak, and K. Parida, "Review on MXene/TiO_2 Nanohybrids for Photocatalytic Hydrogen Production and Pollutant Degradations," *Journal of Environmental Chemical Engineering* 10 (2022): 107211, https://doi.org/10.1016/j.jece.2022.107211.

56. U. Amara, I. Hussain, M. Ahmad, et al., "2D MXene-Based Biosensing: A Review," *Small* 19 (2023): 2205249, https://doi.org/10.1002/smll.202205249.

57. A. Ali, S. M. Majhi, L. A. Siddig, et al., "Recent Advancements in MXene-Based *Biosensors* for Health and Environmental Applications—a Review,"*Biosensors* 14 (2024): 497, https://doi.org/10.3390/bios14100497.

58. G. P. Lim, C. F. Soon, A. A. Al-Gheethi, et al., "Recent Progress and New Perspective of MXene-Based Membranes for Water Purification: A Review," *Ceramics International* 48 (2022): 16477, https://doi.org/10.1016/j.ceramint.2022.03.165.

59. A. Hojjati-Najafabadi, M. Mansoorianfar, T. Liang, et al., "Magnetic-MXene-Based Nanocomposites for Water and Wastewater Treatment: A Review," *Journal of Water Process Engineering* 47 (2022): 102696, https://doi.org/10.1016/j.jwpe.2022.102696.

60. J. Yang, Y. Zhang, Y. Song, et al., "Rechargeable Seawater-Based Chloride-Ion Batteries Enabled by Covalent Surface Chemistry in MXenes," *Journal of the American Chemical Society* 146 (2024): 25680–25688, https://doi.org/10.1021/jacs.4c07809.

61. M. Zhu, D. Ye, X. Liao, et al., "Interface Engineering via High-Entropy Sulfides for Synergistic Modulation of Lithium Nucleation and SEI

25666223, 2026, 9, Downloaded from https://chemistry-europe.onlinelibrary.wiley.com/doi/10.1002/batt.70466 by Politecnico Di Torino Sist. Bibl Del Polit Di Torino, Wiley Online Library on [29/10/2026]. See the Terms and Conditions (https://onlinelibrary.wiley.com/terms-and-conditions) on Wiley Online Library for rules of use; OA articles are governed by the applicable Creative Commons License

Stability Toward Ultra-Stable Lithium Metal Anodes," *Energy Storage Materials* 89 (2026): 105256, https://doi.org/10.1016/j.ensm.2026.105256.

62. M. Zhu, C. Cai, X. Li, et al., "Interfacial MXene Engineering Enabled Lamellar Lithium Nucleation for Dendrite-Free Lithium Anodes," *Journal of Power Sources* 633 (2025): 236451, https://doi.org/10.1016/j.jpowsour.2025.236451.

63. C. Gao, J. Kang, Y. Zhang, et al., "Advances in Anode Current Collectors With a Lithiophilic Gradient for Lithium Metal Batteries," *Chemical Communications* 60 (2024): 9130–9148, https://doi.org/10.1039/d4cc02324b.

64. J. Luo, C. Wang, H. Wang, et al., "Pillared MXene With Ultralarge Interlayer Spacing as a Stable Matrix for High Performance Sodium Metal Anodes," *Advanced Functional Materials* 29 (2019): 1805946, https://doi.org/10.1002/adfm.201805946.

65. E. Cha, J. H. Yun, R. Ponraj, et al., "A Mechanistic Review of Lithiophilic Materials: Resolving Lithium Dendrites and Advancing Lithium Metal-Based Batteries," *Materials Chemistry Frontiers* 5 (2021): 6294–6314, https://doi.org/10.1039/d1qm00579k.

66. I. Ostroman, C. Ferrara, S. Marchionna, et al., "Highly Reversible Ti/Sn Oxide Nanocomposite Electrodes for Lithium Ion Batteries Obtained by Oxidation of Ti_3 $Al_{(1-x)}$ Sn_x C_2 Phases," *Small Methods* 7 (2023): 2300503, https://doi.org/10.1002/smtd.202300503.

67. F. Robert, P. E. Lippens, J. Olivier-Fourcade, et al., "Mössbauer Spectra as a "Fingerprint" in Tin–lithium Compounds: Applications to Li-Ion Batteries," *Journal of Solid State Chemistry* 180 (2007): 339–348, https://doi.org/10.1016/j.jssc.2006.10.026.

68. I. Ostroman, N. Vallana, A. Gentile, et al., "Tailoring Oxide/MAX Phase Nanocomposites via Low-Temperature Oxidation for Lithium-Ion Battery Anodes: Peeking Behind the Electrochemical Mechanism via In Situ Investigations," *Advanced Science* 12 (2025): e12947, https://doi.org/10.1002/advs.202512947.

69. B. D. Adams, J. Zheng, X. Ren, et al., "Accurate Determination of Coulombic Efficiency for Lithium Metal Anodes and Lithium Metal Batteries," *Advanced Energy Materials* 8 (2018): 1702097, https://doi.org/10.1002/aenm.201702097.

70. A. Gentile, S. Marchionna, M. Balordi, et al., "Critical Analysis of MXene Production With in-Situ HF Forming Agents for Sustainable Manufacturing," *ChemElectroChem* 9 (2022): e202200891, https://doi.org/10.1002/celc.202200891.

71. R. Rakhmanov, S. Ippolito, M. Downes, et al., "Influence of MXene Interlayer Spacing on the Interaction With Microwave Radiation," *Advanced Functional Materials* 35 (2025): 2410591, https://doi.org/10.1002/adfm.202410591.

72. S. De Monredon, A. Cellot, F. Ribot, et al., "Synthesis and Characterization of Crystalline Tin Oxide Nanoparticles," *Journal of Materials Chemistry* 12 (2002): 2396–2400, https://doi.org/10.1039/b203049g.

73. L. Stievano and F. E. Wagner, "*Characterization of Solid Materials and Heterogeneous Catalysts: From Structure to Surface Reactivity*," M. Che, and J. Védrine (Wiley-VCH, 2012), 1181.

74. A. Sarycheva and Y. Gogotsi, "Raman Spectroscopy Analysis of the Structure and Surface Chemistry of $Ti_3C_2T_x$ MXene," *Chemistry of Materials* 32 (2020): 3480–3488, https://doi.org/10.1021/acs.chemmater.0c00359.

75. A. Gentile, N. Pianta, M. Fracchia, et al., "$Ti_3C_2T_x$ MXenes as Anodes for Sodium-Ion Batteries: The In Situ Comprehension of the Electrode Reaction," *ACS Applied Energy Materials* 8 (2025): 2229–2238, https://doi.org/10.1021/acsaem.4c02777.

76. T. Brousse, D. Defives, L. Pasquereau, et al., "Metal Oxide Anodes for Li-Ion Batteries," *Ionics* 3 (1997): 332–337.

77. L. F. Olbrich, N. Pianta, B. Jagger, et al., "Electrochemical Impedance Spectroscopy Investigation of the SEI Formed on Lithium Metal Anodes," *ACS Electrochemistry* 2 (2026): 166–174, https://doi.org/10.1021/ACSELECTROCHEM.5C00388.

78. S. Klink, E. Madej, E. Ventosa, et al., "The Importance of Cell Geometry for Electrochemical Impedance Spectroscopy in Three-Electrode Lithium Ion Battery Test Cells," *Electrochemistry Communications* 22 (2012): 120–123, https://doi.org/10.1016/J.ELECOM.2012.06.010.

79. D. T. Boyle, X. Kong, A. Pei, et al., "Transient Voltammetry With Ultramicroelectrodes Reveals the Electron Transfer Kinetics of Lithium Metal Anodes," *ACS Energy Letters* 5 (2020): 701–709, https://doi.org/10.1021/acsenergylett.0c00031.

80. A. Zaban, E. Zinigrad, and D. Aurbach, "Impedance Spectroscopy of Li Electrodes. 4. A General Simple Model of the Li–Solution Interphase in Polar Aprotic Systems," *Journal of Physical Chemistry* 100 (1996): 3089–3101, https://doi.org/10.1021/JP9514279.

81. S. J. Kim, J. H. Choi, J. C. Choi, et al., "Balanced 3D Host Structure of Graphitic Carbon, Amorphous Carbon, and SnO_2 for Uniform and Stable Lithium Deposition in Lithium Metal Anodes," *Carbon* 243 (2025): 120497, https://doi.org/10.1016/j.carbon.2025.120497.

82. C. Dong, H. Shi, H. Cui, et al., "Large-Area Dendrite-Free Ultrathin Li-Rich 3D Li-Sn Alloy/Graphene Foil for High-Performance All-Solid-State Lithium-Sulfur Batteries," *Energy Storage Materials* 75 (2025): 103987, https://doi.org/10.1016/j.ensm.2024.103987.

83. Y. An, Y. Tian, Y. Zhang, et al., "Two-Dimensional Silicon/Carbon From Commercial Alloy and CO_2 for Lithium Storage and Flexible $Ti_3C_2T_x$ MXene-Based Lithium-Metal Batteries," *ACS Nano* 14 (2020): 17574–17588, https://doi.org/10.1021/acsnano.0c08336.

84. J. Yoon, O. B. Chae, M. Wu, et al., "Dual-Functional Surface of MXene Anodes Boosts Long-Term Cyclability of Lithium-Metal Batteries," *Journal of Materials Chemistry A* 13 (2025): 17511–17518, https://doi.org/10.1039/d5ta00519a.

Supporting Information

Additional supporting information can be found online in the Supporting Information section.

25666223, 2026, 9, Downloaded from https://chemistry-europe.onlinelibrary.wiley.com/doi/10.1002/batt.70466 by Politecnico Di Torino Sist. Bibl Del Polit Di Torino, Wiley Online Library on [29/10/2026]. See the Terms and Conditions (https://onlinelibrary.wiley.com/terms-and-conditions) on Wiley Online Library for rules of use; OA articles are governed by the applicable Creative Commons License